Article ID: 1000-324X(2023)09-1103-07 **DOI:** 10.15541/jim20230002

Effect of Film Formation Processes of NiO_x Mesoporous Layer on Performance of Perovskite Solar Cells with Carbon Electrodes

FANG Wanli[1,2], SHEN Lili[2], LI Haiyan[2], CHEN Xinyu[2], CHEN Zongqi[2], SHOU Chunhui[3], ZHAO Bin[1], YANG Songwang[1,2,4]

(1. School of Materials and Chemistry, University of Shanghai for Science and Technology, Shanghai 200093, China; 2. CAS Key Laboratory of Materials for Energy Conversion, Shanghai Institute of Ceramics, Chinese Academy of Sciences, Shanghai 201899, China; 3. Key Laboratory of Solar Energy Utilization & Energy Saving Technology of Zhejiang Province, Zhejiang Energy Group R&D, Hangzhou 310003, China; 4. Center of Materials Science and Optoelectronics Engineering, University of Chinese Academy of Sciences, Beijing 100049, China)

Abstract: Carbon-based perovskite solar cells (C-PSCs) play an important role in industrialization research due to their stability and low cost. In this work, high-quality NiO_x mesoporous layer was selected as a hole transport layer (HTL) based on $MAPbI_3$ material to enhance the performance of C-PSCs. The effect of preparation methods of the NiO_x mesoporous layer on the solar cell performance and the optimum thickness of the NiO_x mesoporous layer were investigated. It was found that mesoporous layers prepared by screen-printing process with well-distributed pores facilitated the filling of perovskite (PVK) precursor solution in the underlayer mesoporous scaffold. Finally, an HTL-contained perovskite solar cell with high efficiency and almost negligible hysteresis was achieved, possessing an open-circuit voltage (V_{OC}) of 910 mV, a power conversion efficiency (PCE) of 14.63%, and certified efficiency reached 14.88%. Moreover, PCE of the solar cell displayed outstanding stability after being stored in air for nearly 900 h.

Key words: carbon-based perovskite solar cell; NiO_x hole transport layer; pore distribution; stability

In the past decade, PCE of PSCs has achieved 25.7%[1]. However, commercializing PSCs is still challenging due to the issues of large-area preparation and long-term stability[2], which C-PSCs hold promise to address[3]. HTL-free C-PSCs exhibit lower efficiency compared to metal-based devices due to the energy level mismatching (0.4 eV) between valence band maximum (VBM) of $MAPbI_3$ (–5.4 eV) and carbon electrode (–5.0 eV)[4], which is unfavorable for the hole extraction. Additionally, the ineffective charge extraction and increased charge recombination derive from poor PVK/carbon interface contact. Therefore, it's necessary to develop an effective, low-cost and highly stable p-type inorganic HTL such as CuSCN, NiO_x and MoO_x[5-7] to construct a normal n-i-p structured C-PSC[8].

In 2015, NiO_x mesoporous layer was firstly deposited on the insulating ZrO_2 or Al_2O_3 layer to establish PSC with normal n-i-p structure, and PCE of 14.9%[9] and 15.03%[10] was achieved respectively. However, PCE of the NiO_x based n-i-p structured C-PSCs with $MAPbI_3$ materials is not satisfactory during subsequent research. Since superior conductivity and zero band gap characteristics of graphene can be exploited to improve device performance[11], Tao, *et al*[12] modified HTL by using NiO_x/graphene to achieve a PCE of 11.72%. Bhandari, *et al*[13] enhanced the efficiency of C-PSCs to 14.2% by further optimizing the carbon electrode. However, there are no relevant studies that relate the quality of mesoporous NiO_x films to the performance of C-PSCs.

In order to improve PCE of NiO_x-based C-PSCs, NiO_x mesoporous layer with uniform thickness and well-distributed pores is necessary. In this work, spin-coating and screen-printing processes were used to prepare NiO_x mesoporous films to investigate the effect of film formation processes of NiO_x mesoporous layer on the performance of C-PSCs.

Received date: 2023-01-01; **Revised date:** 2023-04-11; **Published online:** 2023-04-28
Foundation item: Natural Science Foundation of Shanghai (21ZR1445700); The Key R&D Program of Zhejiang Province (2021C04009)
Biography: FANG Wanli (1997–), female, Master candidate. E-mail: fangwl08@163.com
方万丽(1997–), 女, 硕士研究生. E-mail: fangwl08@163.com
Corresponding author: ZHAO Bin, professor. E-mail: zhaobin@usst.edu.cn; YANG Songwang, professor. E-mail: swyang@mail.sic.ac.cn
赵 斌, 教授. E-mail: zhaobin@usst.edu.cn; 杨松旺, 研究员. E-mail: swyang@mail.sic.ac.cn

1 Experimental

1.1 Materials

Ethanol (EtOH, 95%) and 4-hydroxybutanoic acid lactone (GBL, 99.99%) were purchased from Aladdin Reagent. Lead iodide (PbI_2, 99.99%) was purchased from Xi'an Polymer Light Technology Corp. Methylammonium iodide (MAI, 99.9%) and 5-ammonium valeric acid iodide (5-AVAI) were purchased from Greatcell Solar. $Ni(NO_3)_2{\cdot}6H_2O$ was purchased from Sigma-Aldrich. NaOH (99.99%) was purchased from Aladdin Reagent. All chemicals were used without further purification.

1.2 Preparation of NiO_x nanoparticles

NiO_x nanoparticles were synthesized by a chemical precipitation method[14]. $Ni(NO_3)_2{\cdot}6H_2O$ (0.5 mol) was dispersed in deionized water (100 mL), and pH of the solution was adjusted to 10 by adding NaOH solution (10 mol/L). After stirring for 15 min, the colloidal precipitation was washed with deionized water and dried at 80 ℃ for 6 h. Then it was calcined at 270 ℃ for 2 h. Finally, the synthesized nanoparticles were dispersed in deionized water. For the screen-printing paste, it was prepared with ethyl cellulose as the binder and terpineol as the solvent.

1.3 Preparation of perovskite solution

PbI_2 (0.5761 g), MAI (0.1953 g), and 5-AVAI (0.0152 g) were dissolved in a mixed solution of GBL (800 μL) and EtOH (200 μL).

1.4 Device fabrication

The FTO glass substrates were etched by laser and cleaned sequentially in detergent, deionized water, and ethanol for 60 min. Then, a dense TiO_2 blocking layer, followed by mesoporous TiO_2, ZrO_2, NiO_x (or 60 μL, 3000 r/min, 60 s for spin-coating process), and carbon layers were screen-printed in sequence. Each layer was dried at 100 ℃ for 10 min, and annealed at 510 ℃ for 30 min (except for the carbon layer which was annealed at 430 ℃ for 30 min). Finally, perovskite solution was dropped onto the carbon layer and annealed at 50 ℃ for 60 min. The derived devices were labeled as device A (TiO_2/ZrO_2/carbon), device B ($TiO_2/ZrO_2/NiO_x$(spin-coated)/carbon), and device C ($TiO_2/ZrO_2/NiO_x$(screen-printed)/carbon), respectively.

2 Results and discussion

The device structure is FTO/$TiO_2/ZrO_2/NiO_x$/carbon with PVK grains filled in the mesoporous scaffold in Fig. 1(a). Fig. 1(b) indicates that VBM of NiO_x (–5.2 eV) matches well with $MAPbI_3$ (–5.4 eV) due to its lower energy level than carbon (–5.0 eV)[15]. Thus, the existence of NiO_x layer provides a better energy band alignment with PVK, which is beneficial to the extraction of holes.

This work compared spin-coating and screen-printing methods to achieve high-quality NiO_x mesoporous films. XRD pattern of synthesized NiO_x nanoparticles is shown in Fig. S1. Fig. 1(c-e) present the cross-sectional SEM images of different devices. It can be observed that the thicknesses of the carbon layers are almost the same for all devices (Fig. S2). Fig. 1(f) confirms the successful deposition of different mesoporous layers through the element distribution mapping of Ti, Zr, Ni, and Pb. Moreover, the relative homogeneity of the lead signal intensity in the profile indicates that the perovskite is uniformly filled in the scaffold. In Fig. 1(d, e), it's obvious that the NiO_x layer deposited by spin-coating is too thin to be identified, possibly due to the dispersed

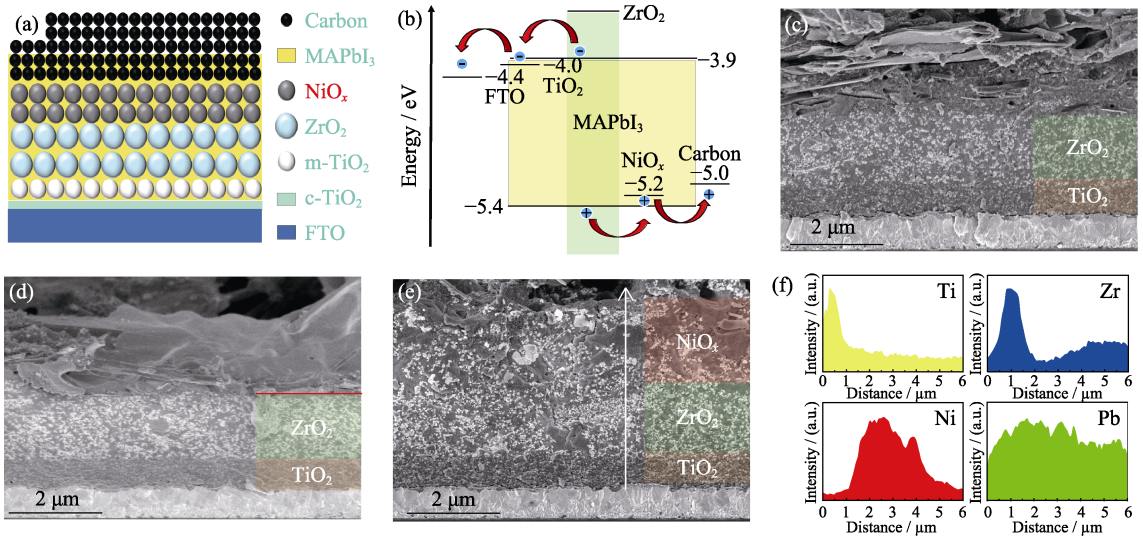

Fig. 1 (a) Schematic illustration and (b) work function of the device, cross-sectional SEM images of C-PSCs: (c) device A, (d) device B and (e) device C, and (f) element distribution in the direction of the white arrow in (e)

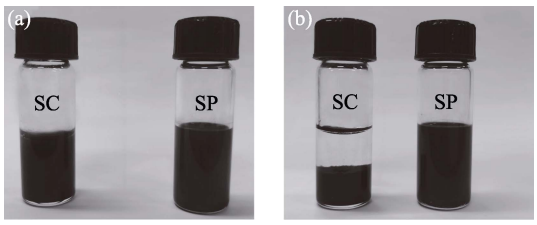

Fig. 2　Photographs of NiO_x dispersions for (left) spin-coating (SC), for (right) screen-printing (SP) (a) before and (b) after standing for 30 min

NiO_x nanoparticles in deionized water penetrating the hollows in the ZrO_2 underlay. To confirm this, the NiO_x nanoparticle dispersion and the screen-printable paste were left to stand for 30 min, respectively. The NiO_x nanoparticle dispersion for spin-coating was observed to precipitate after 30 min of storage, while the screen-printable paste remained well-dispersed without any delamination, as shown in Fig. 2. This is attributed to the difference in solvents and binders used for the spin-coating NiO_x dispersion and screen-printing NiO_x paste.

The top view SEM images of the ZrO_2 film, spin-coated, and screen-printed NiO_x mesoporous films are presented in Fig. 3(a-c), respectively. The high-magnification SEM images of the screen-printed ZrO_2 and NiO_x film are placed in Fig. S3. It is worth noting that the screen-printed NiO_x film has well-distributed pores, which benefits the penetration of the perovskite precursor solution, while the spin-coated NiO_x film has poor coverage and a relatively dense surface. To investigate the effect of the NiO_x mesoporous layer on charge extraction, photoluminescence (PL) tests were carried out. The results in Fig. 3(d) show that the PL emission is

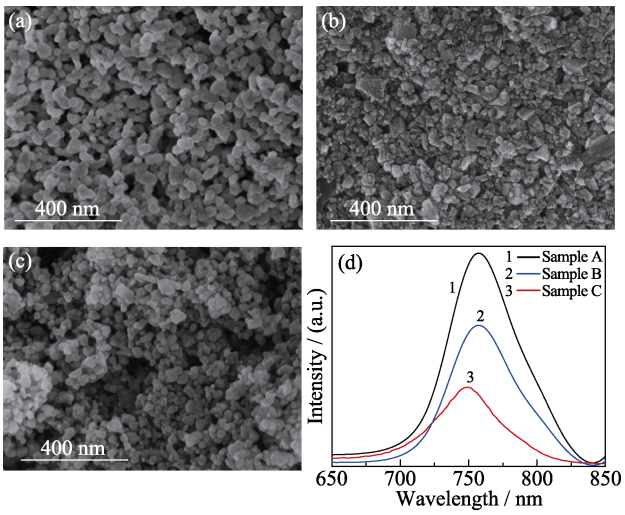

Fig. 3　SEM images of (a) ZrO_2 mesoporous film, (b) spin-coated and (c) screen-printed NiO_x films, and (d) PL spectra for sample A (ZrO_2/$MAPbI_3$), sample B (ZrO_2/NiO_x (spin-coated)/$MAPbI_3$), and sample C (ZrO_2/NiO_x(screen-printed)/$MAPbI_3$)

significantly suppressed with the insertion of the NiO_x mesoporous layer, especially for sample C (ZrO_2/NiO_x(screen-printed)/$MAPbI_3$), which means more efficient hole extraction in ZrO_2/NiO_x/$MAPbI_3$ interface. Moreover, the PL peak of sample C exhibits a slight blue shift compared to the other samples, indicating decreased trap state and reduced defect density of $MAPbI_3$ film[16].

To investigate whether NiO_x mesoporous layer affects the crystallinity of $MAPbI_3$, XRD patterns of devices were carried out. The diffraction peak at 2θ=26.4° corresponds to SnO_2 of the FTO substrate (Fig. 4(a)). Device C has the narrowest half-peak width of (110) plane implying large grains (Fig. 4(b)), possibly due to its large pores for the permeation and crystallization of perovskite grains. It should be noted that the valence state of Ni affects the interfacial oxidation and thus the recombination of carriers[17]. In this work, the effect of the valence state of Ni is similar due to the same post-treatment processes for NiO_x mesoporous films.

The current density-voltage (*J-V*) curves and photovoltaic parameters of different devices are shown in Fig. 5(a) and Table S1, respectively. The high quality NiO_x HTL can significantly improve V_{OC} and slightly improve J_{SC} compared to device A. Device A shows the worst performance with a PCE of 11.62%, which may be due to poor interface contact and energy level mismatching at the PVK/carbon interface. It is concluded that the quality of the NiO_x HTL affects the efficiency of the device. PCEs of Device C and B achieved 13.49% and 11.78%, respectively. The hysteresis index (HI) was calculated using equation (1)[18] to describe the hysteresis behavior of PSCs.

$$HI=\frac{PCE_{reverse}-PCE_{forward}}{PCE_{reverse}} \quad (1)$$

Device C has the lowest HI of 0.0067, indicating negligible *J-V* hysteresis, compared to device A (HI=0.1472) and device B (HI=0.0119). The spin-coated NiO_x HTL does not apparently enhance the performance

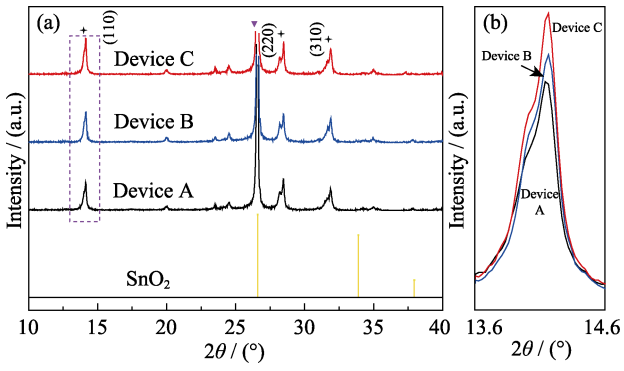

Fig. 4　(a) XRD patterns of $MAPbI_3$ in different devices and (b) local magnified XRD patterns in range of 13.6°–14.6°

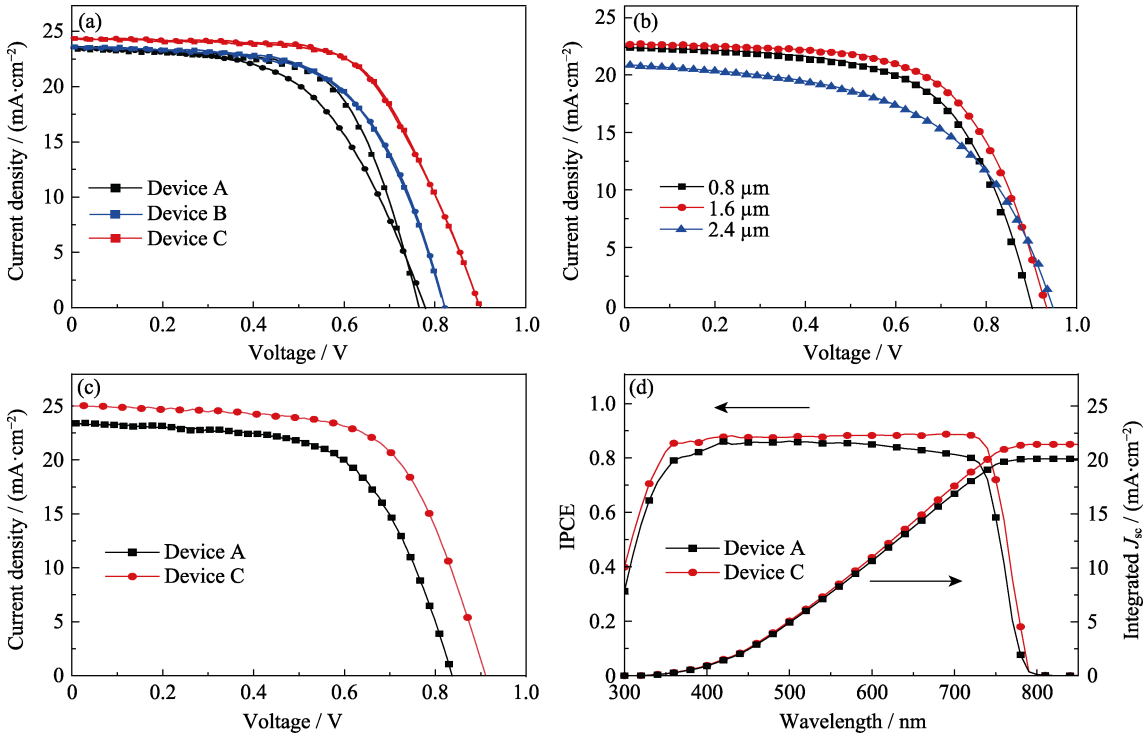

Fig. 5 (a-c) *J-V* curves and (d) incident photon-to-electron conversion efficiency (IPCE) spectra and the integrated current density curves of different devices

(a) Forward and reverse scans of device A, B and C; (b) Different thicknesses of NiO_x layer; (c) The optimum cells of device A and device C; Colorful figures are available on website

of C-PSCs. So, device A and device C were compared subsequently.

The thickness of the screen printed NiO_x mesoporous layer has a decisive influence on PVK/carbon interface and series resistance, and the highest PCE was achieved when the thickness was 1.6 μm (Fig. 5(b)). A reduction in thickness is not conducive to interfacial contact, while an increase in thickness increases series resistance. Table S2 lists the specific photovoltaic parameters.

Fig. 5(c) presents *J-V* curves of the optimum devices. Their corresponding photovoltaic parameters are shown in Table S3. Device A exhibited PCE of 11.95% with V_{OC} of 0.840 V, J_{SC} of 23.39 mA·cm^{-2}, and FF of 0.61. While device C exhibited PCE of 14.63% with V_{OC} of 0.910 V, J_{SC} of 25.04 mA·cm^{-2}, and FF of 0.64. Improvements of J_{SC} by 7.1% and FF by 5.1% were observed when the high quality NiO_x mesoporous layer is employed. The increase in device efficiency is mostly due to the increment in V_{OC}, from 840 mV to 910 mV. Fig. 5(d) shows the corresponding IPCE spectra and integrated current density curves of the devices. Compared with device A, device C has higher IPCE over the whole wavelength ranging from 300 nm to 850 nm, illustrating more efficient utilization of sunlight for C-PSCs. However, the value of integrated current density is lower than that of *J-V* test, probably because the device is not fully activated, which is related to light intensity[19]. The performance of devices was further testified for certification measurement with PCE=14.88%, V_{OC}=0.882 V, I_{SC}=1.87 mA, and FF=63.19% (Fig. S4), which indicates the reliability of laboratory results and superior performance of this work.

The dark *J-V* curves of devices in Fig. 6(a) can provide important information, such as shunt resistance (R_{sh}), series resistance (R_s), leakage current, and diode characteristics. Device C exhibited more ideal diode characteristics compared to device A, and the ideality factor, n can be calculated using the slope and formula (2)[20]:

$$n = \left(\frac{2.303 k_B T \partial \lg I}{q_e \partial V} \right)^{-1} \quad (2)$$

Where k_B=1.380649×10^{-26} J·K^{-1}, q_e=1.6×10^{-19} C, and T represent Boltzmann constant, the elementary charge, and temperature (K), respectively. Here n=1.35 for device C, which is significantly lower than that of 3.01 for device A. Although the p-n junction equivalent circuit is usually used to simulate the perovskite solar cell, it is difficult to directly obtain the potential and n of each diode due to the inhomogeneous built-in electric field. So the overall n is typically used to evaluate the diode characteristics of the device[21-22]. Lower n accounts for the improved diode quality[23]. It can be seen that the dark current density of the device C is almost an order of magnitude lower than that of device A (Fig. 6(a)), implying less current leakage and charge recombination, but increased sheet resistance.

The dependence of V_{OC} on light intensity was tested to

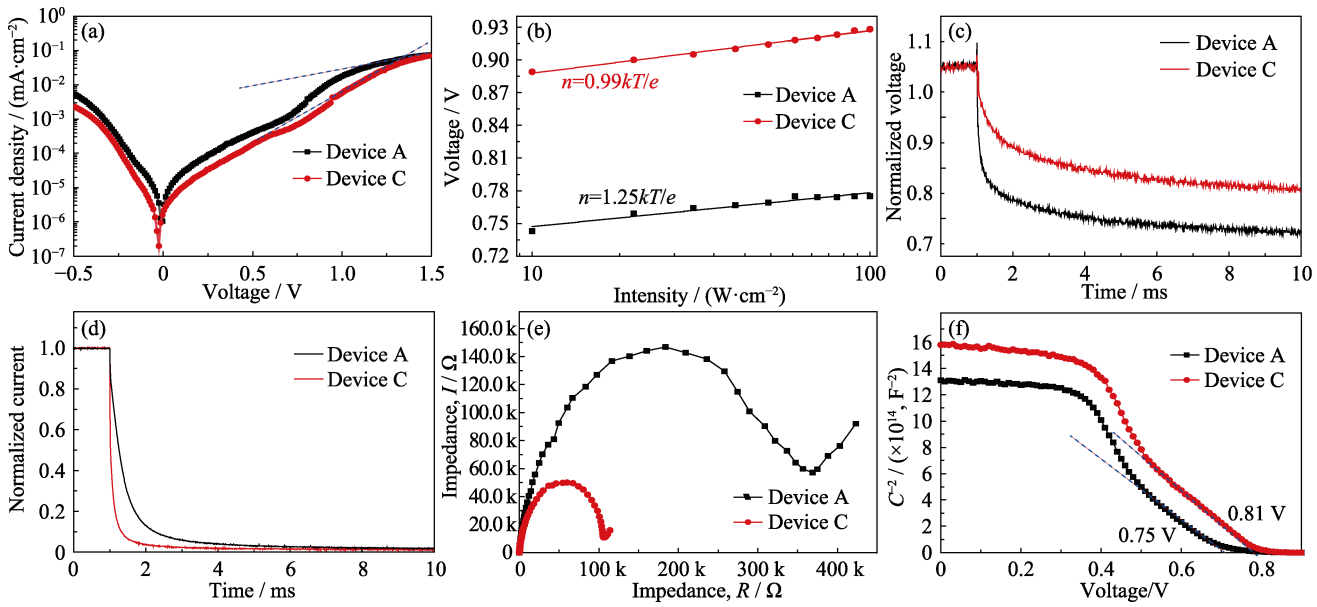

Fig. 6　(a) *J-V* curves under dark conditions, (b) light-intensity dependence of V_{OC} (solid line: linear fitting), (c) transient photovoltage (TPV) decay curves, (d) transient photocurrent (TPC) decay curves, (e) Nyquist plots measured in the dark, and (f) Mott-Schottky plots for device A and device C; Colorful figures are available on website

further investigate the recombination behavior of charge carriers. Fig. 6(b) shows the linear fitting of V_{OC} as a function of logarithmic light intensity (lg*I*) with different slopes. With calculation, n for device A and device C were 0.99 and 1.25, respectively. It is reported that n is related to defect-assisted recombination[24]. This confirms that high quality mesoporous NiO_x film as HTL at PVK/carbon interface can reduce carrier recombination, consistent with PL spectra, which is beneficial to PCE.

The decay of photovoltage and photocurrent can reveal the transport and recombination process of photogenerated carriers. Restricting recombination at the PVK/carbon interface contributed to longer V_{OC} decay time (Fig. 6(c)). The NiO_x mesoporous layer reduces the recombination of photogenerated electrons and holes, thus improving the device's efficiency. Device C displayed a faster decay of photocurrent in the short-circuit state compared to device A in Fig. 6(d), indicating better charge extraction capability, which is attributed to the enhanced hole transport from the perovskite layer to the carbon electrode[25].

Electrochemical impedance spectroscopy (EIS) was used to investigate charge transport and recombination in the devices. The semicircle in the high-frequency range represents the charge transfer resistance (R_{ct}) at the interface, and the semicircle in the low-frequency region represents the charge recombination resistance (R_{rec}) in the device[26]. As shown in Fig. 6(e), device C exhibits smaller semicircle in the high-frequency region and larger semicircle in the low-frequency region, indicating more efficient charge transfer and transport.

Mott-Schottky analysis was conducted to explain the improved V_{OC} in device C. The built-in potential (V_{bi}) of the device was determined by fitting the linear portion of the C^{-2}-V curve using equation (3)[27].

$$\frac{1}{C^2}=\frac{2}{A^2\cdot N\cdot q\cdot\varepsilon\cdot\varepsilon_0}(V_{bi}-V) \tag{3}$$

Where C, A, N, q, ε, ε_0, and V represent capacitance (F), active area (cm^2), the concentration of donor-dopant (cm^{-3}), elementary charge (C), relative permittivity, the permittivity of free space, and applied bias, respectively. It was reported that V_{OC} depends on V_{bi}[28]. In this work, V_{bi} is 0.81 V for device C and 0.75 V for device A. It is concluded that high quality NiO_x mesoporous layer optimizes the energy level arrangement, enhances the built-in potential, and reduces the loss of V_{OC} in the device.

Stability is a crucial factor for the commercialization of PSCs. C-PSCs are more stable due to the hydrophobic nature of carbon electrodes. Unencapsulated devices were stored for nearly 900 h, and their evolution in J_{SC}, V_{OC}, FF, and PCE were monitored in Fig. 7(a-d). At the initial 20 h, all parameters, except J_{SC} of device C, increased possibly due to further crystallization of perovskite grains induced by solvent evaporation. Both devices' V_{OC} increased due to the recrystallization of filled perovskite in mesopores under the combined action of water and oxygen[29]. J_{SC} decreased over time, while the general trend of the evolution of FF and PCE was similar. NiO_x-based C-PSCs showed better stability than C-PSCs without HTL.

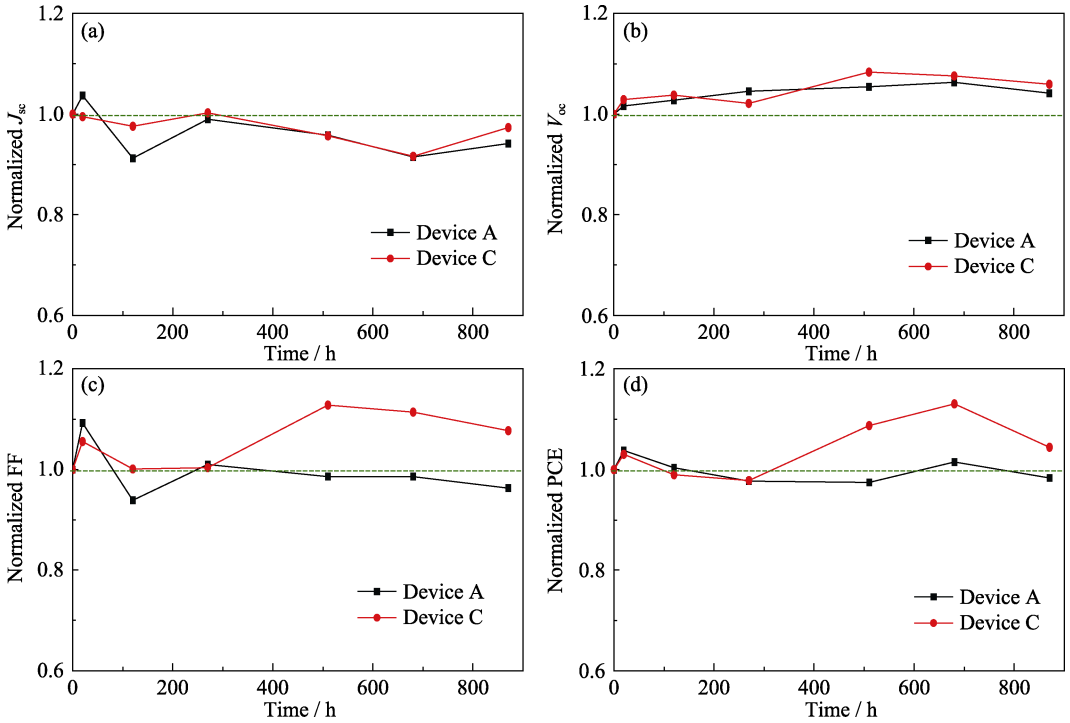

Fig. 7 Long-term storage stability of PSCs in air with relative humidity of 30%–40%
(a) J_{SC}; (b) V_{OC}; (c) FF; (d) PCE

3 Conclusions

This work demonstrates the importance of the film formation process of the p-type NiO_x mesoporous layer in improving the efficiency and stability of C-PSCs. The results show that the NiO_x mesoporous film prepared by screen-printing progress with well-distributed pores allows for better penetration of the perovskite precursor solution, leading to a significant improvement in efficiency of C-PSCs from 11.95% to 14.63%, with a certified efficiency of 14.88%. Additionally, the device maintains its efficiency for nearly 900 h without degradation. These findings have important implications for the commercialization of C-PSCs.

Supporting materials

Supporting materials related to this article can be found at https://doi.org/10.15541/jim20230002.

References:

[1] KIM M, JEONG J, LU H, *et al.* Conformal quantum dot-SnO_2 layers as electron transporters for efficient perovskite solar cells. *Science*, 2022, **375(6578):** 302.

[2] SAMANTARAY M R, RANA N K, KUMAR A, *et al.* Stability study of large-area perovskite solar cells fabricated with copper as low-cost metal contact. *J. Energy Res.*, 2022, **46(2):** 1250.

[3] YUE M, YUE H, ANYI M, *et al.* Application of lead acetate additive for printable perovskite solar cell. *J. Inorg. Mater.*, 2022, **37(2):** 197.

[4] LAURA M G, DANIEL R, FRANKLIN J. Current status and trends of carbon-based electrodes for fully solution-processed perovskite solar cells. *J. Energy Chem.*, 2021, **68:** 222.

[5] LIU S, HUANG W, LIAO P, *et al.* 17% efficient printable mesoscopic PIN metal oxide framework perovskite solar cells using cesium-containing triple cation perovskite. *J. Mater. Chem. A*, 2017, **5(44):** 22952.

[6] JAYAN K D, SEBASTIAN V. Comprehensive device modelling and performance analysis of $MASnI_3$ based perovskite solar cells with diverse ETM, HTM and back metal contacts. *Sol. Energy*, 2021, **217:** 40.

[7] WANG J, ZHENG Z, ZU Y, *et al.* A tandem organic photovoltaic cell with 19.6% efficiency enabled by light distribution control. *Adv. Mater.*, 2021, **33(39):** 2102787.

[8] WANG H, HUANG Z, XIAO S, *et al.* An *in situ* bifacial passivation strategy for flexible perovskite solar module with mechanical robustness by roll-to-roll fabrication. *J. Mater. Chem. A*, 2021, **9(9):** 5759.

[9] XU X, LIU Z, ZUO Z, *et al.* Hole selective NiO contact for efficient perovskite solar cells with carbon electrode. *Nano Lett.*, 2015, **15(4):** 2402.

[10] CAO K, ZUO Z, CUI J, *et al.* Efficient screen printed perovskite solar cells based on mesoscopic $TiO_2/Al_2O_3/NiO$/carbon architecture. *Nano Energy*, 2015, **17:** 171.

[11] LIU X, REN S, LI Z, *et al.* Flexible transparent high-efficiency photoelectric perovskite resistive switching memory. *Adv. Funct. Mater.*, 2022, **32(38):** 2202951.

[12] TAO L, ZHANG Y, CHEN H, *et al.* Printable commercial carbon based mesoscopic perovskite solar cell using NiO/graphene as hole-transport materials. *ECS J. Solid State Sci. Technol.*, 2021, **10(10):** 105003.

[13] BHANDARI S, ROY A, ALI M S, *et al.* Cotton soot derived carbon nanoparticles for NiO supported processing temperature tuned ambient perovskite solar cells. *Sci. Rep.*, 2021, **11:** 23388.

[14] JIANG F, CHOY W C H, LI X, *et al.* Post-treatment-free solution-processed non-stoichiometric NiO_x nanoparticles for efficient hole-transport layers of organic optoelectronic devices. *Adv. Mater.*, 2015, **27(18):** 2930.
[15] LEE J H, JIN I S, JUNG J W. Binary-mixed organic electron transport layers for planar heterojunction perovskite solar cells with high efficiency and thermal reliability. *Chem. Eng. J.*, 2021, **420:** 129678.
[16] HOU X M, HU Y, LIU H W, *et al.* Effect of guanidinium on mesoscopic perovskite solar cells. *J. Mater. Chem. A*, 2017, **5(1):** 73.
[17] ZHAO J J, SU X, MI Z, *et al.* Trivalent Ni oxidation controlled through regulating lithium content to minimize perovskite interfacial recombination. *Rare Metals*, 2022, **41(1):** 96.
[18] LIU Z, SUN B, LIU X, *et al.* Efficient carbon-based $CsPbBr_3$ inorganic perovskite solar cells by using Cu-phthalocyanine as hole transport material. *Nano-Micro Lett.*, 2018, **10(2):** 34.
[19] TSUJI R, BOGACHUK D, LUO B, *et al*. Activation of weak monochromic photocurrents by white light irradiation for accurate IPCE measurements of carbon-based multi-porous-layered-electrode perovskite solar cells. *Electrochemistry*, 2020, **88(5):** 418.
[20] LIU X, CHENG Y, LIU C, *et al.* 20.7% highly reproducible inverted planar perovskite solar cells with enhanced fill factor and eliminated hysteresis. *Energy Environ. Sci.*, 2019, **12(5):** 1622.
[21] LIAO P, ZHAO X, LI G, *et al.* A new method for fitting current-voltage curves of planar heterojunction perovskite solar cells. *Nano-Micro Lett.*, 2018, **10:** 5.
[22] KE W, FANG G, WAN J, *et al.* Efficient hole-blocking layer-free planar halide perovskite thin-film solar cells. *Nat. Commun.*, 2015, **6:** 6700.
[23] WANG Y, MAHMOUDI T, HAHN Y B. Highly stable and efficient perovskite solar cells based on FAMA-perovskite-Cu:NiO composites with 20.7% efficiency and 80.5% fill factor. *Adv. Energy Mater.*, 2020, **10(27):** 2000967.
[24] LEGUY A M A, FROST J M, MCMAHON A P, *et al.* The dynamics of methylammonium ions in hybrid organic-inorganic perovskite solar cells. *Nat. Commun.*, 2015, **6:** 7124.
[25] CAI C, ZHOU K, GUO H, *et al.* Enhanced hole extraction by NiO nanoparticles in carbon-based perovskite solar cells. *Electrochim. Acta*, 2019, **312:** 100.
[26] LIU S, LI S, WU J, *et al.* Amide additives induced a Fermi level shift to improve the performance of hole-conductor-free, printable mesoscopic perovskite solar cells. *J. Phy. Chem. Lett.*, 2019, **10(21):** 6865.
[27] LI X, ZHANG W, GUO X, *et al.* Constructing heterojunctions by surface sulfidation for efficient inverted perovskite solar cells. *Science*, 2022, **375(6579):** 434.
[28] ZHOU Y, ZHANG X, LU X, *et al.* Promoting the hole extraction with Co_3O_4 nanomaterials for efficient carbon-based $CsPbI_2Br$ perovskite solar cells. *Solar RRL*, 2019, **3(4):** 1800315.
[29] CHEN X, LU L, GU D, *et al.* Chlorine management of a carbon counter electrode for high performance printable perovskite solar cells. *J. Mater. Chem. C*, 2021, **9(27):** 8615.

NiO_x 介孔层的成膜过程对碳电极钙钛矿太阳能电池性能的影响

方万丽[1,2], 沈黎丽[2], 李海艳[2], 陈薪羽[2], 陈宗琦[2],
寿春晖[3], 赵 斌[1], 杨松旺[1,2,4]

(1. 上海理工大学 材料与化学学院, 上海 200093; 2. 中国科学院 上海硅酸盐研究所, 中国科学院能量转换材料重点实验室, 上海 201899; 3. 浙江省能源集团有限公司 浙江省太阳能利用与节能技术重点实验室, 杭州 310003; 4. 中国科学院大学 材料科学与光电工程中心, 北京 100049)

摘 要: 碳基钙钛矿太阳能电池(C-PSCs)具有稳定性好且成本低的优势, 展现出广阔的应用前景。本研究基于 $MAPbI_3$ 材料, 选择高质量的 NiO_x 介孔层作为空穴传输层(HTL), 对比了 NiO_x 介孔层不同制备方法对电池性能的影响, 并对 NiO_x 介孔层的厚度进行优化。研究发现, 与旋涂工艺制备的 NiO_x 介孔层相比, 丝网印刷工艺制备的介孔层的孔径分布均匀, 可改善钙钛矿(PVK)前体溶液填充在介孔支架中的填充状态。最终得到含 HTL 的高效率和低滞后的钙钛矿太阳能电池, 其开路电压(V_{OC})为 910 mV, 光电转换效率(PCE)为 14.63%, 认证效率达 14.88%。此外, 在空气中储存近 900 h, 其 PCE 没有明显衰减。

关 键 词: 碳电极钙钛矿太阳能电池; NiO_x 空穴传输层; 孔分布; 稳定性

中图分类号: TQ174　　**文献标志码:** A

Supporting materials:

Effect of Film Formation Processes of NiO_x Mesoporous Layer on Performance of Perovskite Solar Cells with Carbon Electrodes

FANG Wanli[1,2], SHEN Lili[2], LI Haiyan[2], CHEN Xinyu[2], CHEN Zongqi[2], SHOU Chunhui[3], ZHAO Bin[1], YANG Songwang[1,2,4]

(1. School of Materials and Chemistry, University of Shanghai for Science and Technology, Shanghai 200093, China; 2. CAS Key Laboratory of Materials for Energy Conversion, Shanghai Institute of Ceramics, Chinese Academy of Sciences, Shanghai 201899, China; 3. Key Laboratory of Solar Energy Utilization & Energy Saving Technology of Zhejiang Province, Zhejiang Energy Group R&D, Hangzhou 310003, China; 4. Center of Materials Science and Optoelectronics Engineering, University of Chinese Academy of Sciences, Beijing 100049, China)

Characterization

The FE-SEM (Thermo-scientific G4 UC) was used to observe the surface morphology of the NiO_x mesoporous layer prepared by different processes and the cross-sectional morphology of the corresponding devices. The elemental distribution is obtained by energy dispersive X-ray spectroscopy (EDX), which is measured by AMETEK EDAX configured with FE-SEM. Steady-state photoluminescence (PL) spectra were measured by the FluoroMax-4 steady-state fluorescence test system, and the samples were exited at 532 nm and labeled as sample A (ZrO_2/$MAPbI_3$), sample B (ZrO_2/NiO_x(spin-coated)/$MAPbI_3$), and sample C (ZrO_2/NiO_x(screen-printed)/$MAPbI_3$), respectively. The X-ray diffractometer (XRD) was characterized by D8 advance with Cu Kα radiation (40 kV, 40 mA). The photovoltaic parameters were measured under 1 sun illumination (100 mW·cm^{-2}) by a solar simulator (Yamashita Denso YSS-150A). The light intensity is calibrated by a standard silicon solar cell with a filter (BS-520BK, Bunkoh-Keiki Co., Ltd). The effective area is defined as 0.07 cm^2 by using a mask. The incident photon-to-electron conversion efficiency (IPCE) spectra were measured with a test step length of 10 nm by Bunkoh-Keiki's CEP-1500 test system. The dark *I-V*, light-intensity dependence of V_{OC}, transient photovoltage decay curves, transient photocurrent decay curves, electrochemical impedance spectroscopy (EIS), and Mott-Schottky (M-S) were performed on Zahner CIMPS- pro electrochemical workstation.

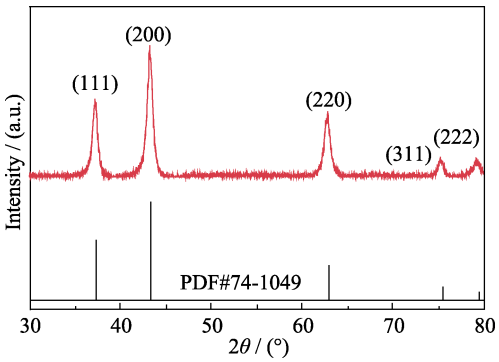

Fig. S1 XRD pattern of NiO_x nanoparticles prepared by chemical precipitation method

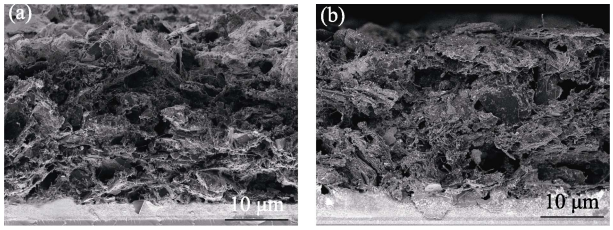

Fig. S2 Low magnification cross-sectional SEM images of (a) device B and (b) device C

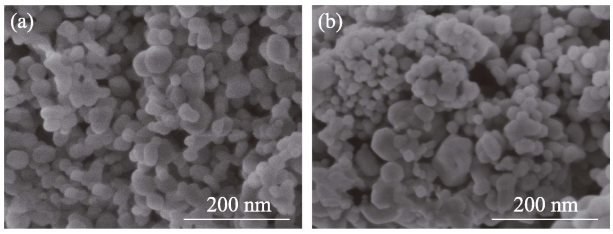

Fig. S3 High magnification top-view SEM images of screen-printed (a) ZrO_2 and (b) NiO_x films

Table S1 Photovoltaic parameters for different devices with an aperture area of 0.07 cm^2 under 1 sun (100 mW·cm^{-2}) illumination

Sample	V_{OC}/V		J_{SC}/(mA·cm^{-2})		FF/%		PCE/%	
	Reverse	Forward	Reverse	Forward	Reverse	Forward	Reverse	Forward
Device A	0.779	0.764	23.45	23.38	63.60	55.47	11.62	9.91
Device B	0.822	0.820	23.62	23.56	60.66	60.26	11.78	11.64
Device C	0.904	0.903	23.57	23.56	63.29	62.98	13.49	13.40

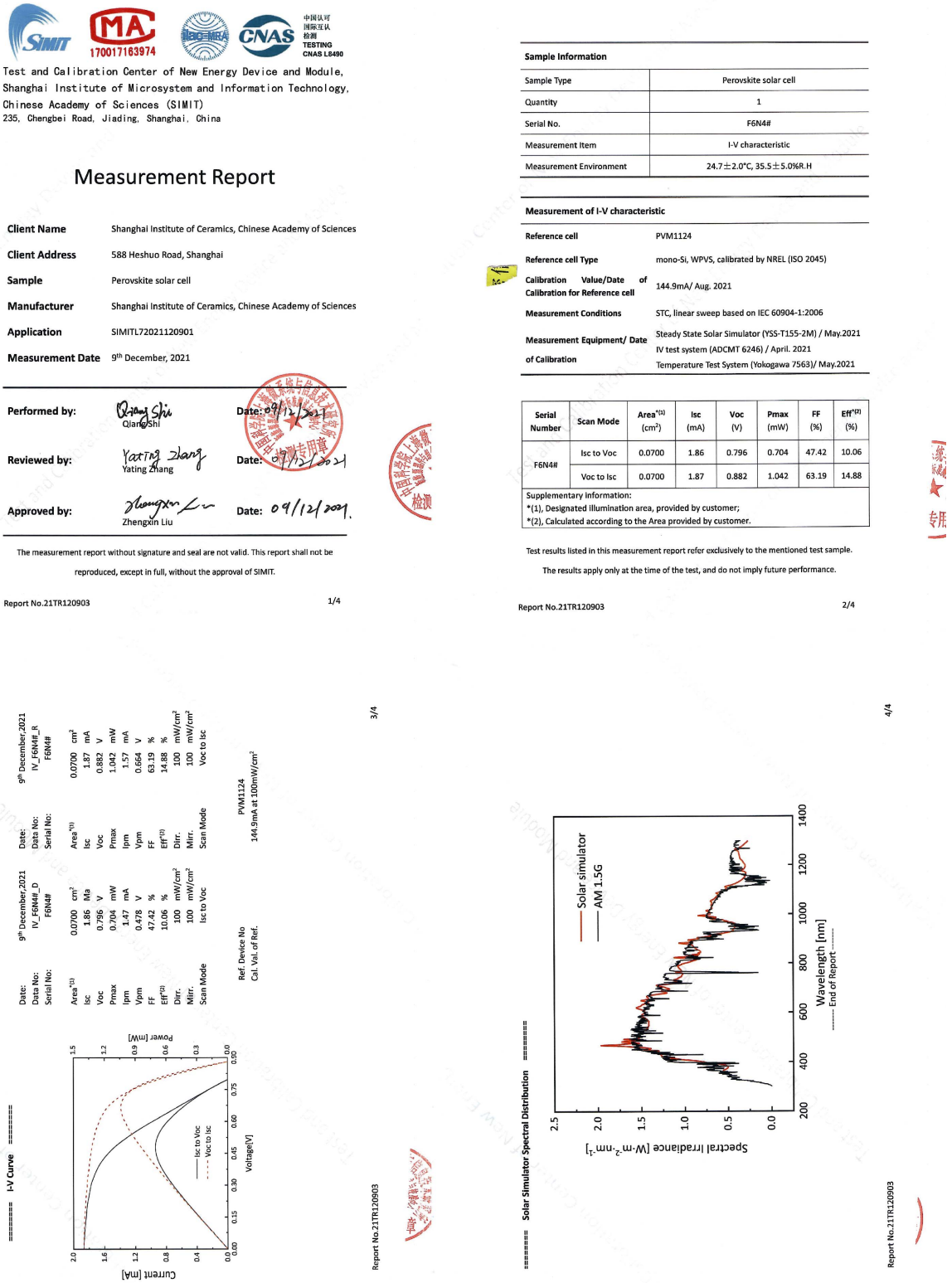

Test and Calibration Center of New Energy Device and Module,
Shanghai Institute of Microsystem and Information Technology,
Chinese Academy of Sciences (SIMIT)
235, Chengbei Road, Jiading, Shanghai, China

Measurement Report

Client Name	Shanghai Institute of Ceramics, Chinese Academy of Sciences
Client Address	588 Heshuo Road, Shanghai
Sample	Perovskite solar cell
Manufacturer	Shanghai Institute of Ceramics, Chinese Academy of Sciences
Application	SIMITL72021120901
Measurement Date	9th December, 2021

Performed by: Qiang Shi　Date: 09/12/2021
Reviewed by: Yating Zhang　Date: 09/12/2021
Approved by: Zhengxin Liu　Date: 09/12/2021

The measurement report without signature and seal are not valid. This report shall not be reproduced, except in full, without the approval of SIMIT.

Report No.21TR120903　1/4

Sample Information	
Sample Type	Perovskite solar cell
Quantity	1
Serial No.	F6N4#
Measurement Item	I-V characteristic
Measurement Environment	24.7±2.0°C, 35.5±5.0%R.H

Measurement of I-V characteristic	
Reference cell	PVM1124
Reference cell Type	mono-Si, WPVS, calibrated by NREL (ISO 2045)
Calibration Value/Date of Calibration for Reference cell	144.9mA/ Aug. 2021
Measurement Conditions	STC, linear sweep based on IEC 60904-1:2006
Measurement Equipment/ Date of Calibration	Steady State Solar Simulator (YSS-T155-2M) / May.2021 IV test system (ADCMT 6246) / April. 2021 Temperature Test System (Yokogawa 7563)/ May.2021

Serial Number	Scan Mode	Area*(1) (cm²)	Isc (mA)	Voc (V)	Pmax (mW)	FF (%)	Eff*(2) (%)
F6N4#	Isc to Voc	0.0700	1.86	0.796	0.704	47.42	10.06
	Voc to Isc	0.0700	1.87	0.882	1.042	63.19	14.88

Supplementary information:
*(1), Designated illumination area, provided by customer;
*(2), Calculated according to the Area provided by customer.

Test results listed in this measurement report refer exclusively to the mentioned test sample.
The results apply only at the time of the test, and do not imply future performance.

Report No.21TR120903　2/4

Report No.21TR120903　3/4

Report No.21TR120903　4/4

Fig. S4　Certified efficiency measurement report of device C

Table S2　Photovoltaic parameters of devices with different thicknesses of screen-printed NiO_x layer

Sample	V_{OC}/V	J_{SC}/(mA·cm^{-2})	FF/%	PCE/%
NiO_x (0.8 μm)	0.898	22.36	61.66	12.38
NiO_x (1.6 μm)	0.932	22.68	62.87	13.28
NiO_x (2.4 μm)	0.939	20.86	54.43	10.66

Table S3　Photovoltaic parameters of device A and C

Device	V_{OC}/V	J_{SC}/(mA·cm^{-2})	FF/%	PCE/%
Device A	0.840	23.39	61.00	11.95
Device C	0.910	25.04	64.13	14.63